

Group: Magnetohydrodynamic

## Magnetohydrodynamics for liquid-metal blankets

*L. Bühler, H.-J. Brinkmann, C. Courtessole, V. Klüber, C. Köhly, C. Mistrangelo*

### Introduction

The design of breeding blankets represents a major challenge for fusion reactor engineering due to performance requirements and severe operating conditions in terms of heat load and neutron flux. Liquid metal alloys such as lead lithium PbLi are considered as breeder material due to their lithium content, as neutron multiplier, and neutron shield. Because of their large thermal conductivity and the possibility to be operated at high temperature, liquid metals may serve additionally as coolants to remove the nuclear heat released in fusion reactors. On the other hand, when the electrically conducting fluid moves in the strong magnetic field that confines the plasma, electric currents are induced. The latter are responsible for strong electromagnetic Lorentz forces and high pressure drop. Magnetohydrodynamic (MHD) pressure drops have to be carefully quantified, since excessive values can jeopardize the feasibility of the considered blanket concept. Moreover, Lorentz forces affect the velocity distribution and suppress turbulence with implications on heat and mass transfer.

The physical parameters characterizing the MHD flow are the Hartmann number, the Reynolds number and the Grashof number

$$Ha = BL\sqrt{\frac{\sigma}{\rho\nu}}, \quad Re = \frac{u_0L}{\nu}, \quad Gr = \frac{g\beta\Delta TL^3}{\nu^2},$$

where  $B$ ,  $L$  and  $u_0$  denote magnetic field, typical length scale and characteristic velocity. The fluid properties are density  $\rho$ , kinematic viscosity  $\nu$ , electric conductivity  $\sigma$  and volumetric thermal expansion coefficient  $\beta$ .

$Ha^2$  and  $Re$  stand for ratios of electromagnetic to viscous forces and inertia to viscous forces,

respectively. The importance of buoyancy forces is quantified by  $Gr$ , where  $\Delta T$  is a typical temperature difference and  $g$  stands for gravity.

The MHD work at ITES KIT supports DEMO blanket engineering activities as part of the EUROfusion consortium and the test blanket program of Fusion For Energy (F4E) for ITER.

### Numerical simulations for liquid metal MHD flows

#### Simulation of 3D MHD flows in pipes with flow channel inserts

When duct walls are thick and electrically conducting, flow-induced currents find shortcuts along these walls, resulting in high current density in the fluid, strong electromagnetic forces and considerable pressure drop. In order to mitigate MHD effects in fusion blankets, electrically insulating flow channel inserts (FCI) have been proposed. They are loosely fitted in liquid metal ducts or pipes with the purpose of electrically decoupling the fluid region from the well-conducting blanket structure. [1]. In the following, a FCI of sandwich-type is considered, as schematically shown in Figure 1, which consists of an insulation layer (orange), enclosed by two thin sheets of steel to protect the insulation from fluid infiltration. Of particular interest are 3D MHD effects present when the flow enters or exits the FCI or at gaps between two FCIs. At these locations current density is locally increased by extra 3D currents  $j_{3D}$ , which affect the flow. This leads to local modifications of electric potential, pressure and velocity. Numerical investigations of complex FCI entry flows at fusion relevant parameters  $Ha = 2000$ ,  $Re = 20000$ , allows to quantify

these 3D effects and provide insight into related experiments performed in the MEKKA laboratory at KIT.

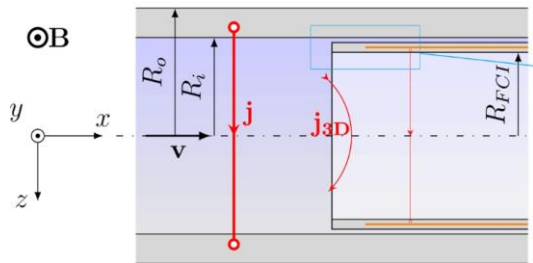


Figure 1 Sketch of the MHD flow entering a FCI, as tested for a circular pipe in the MEKKA laboratory. The orange surface indicates the insulation layer.

The computational model considers the FCI entrance flow at a high degree of geometrical detail, which allows the resolution of wall and conducting sheets of the FCI for determination of currents. The geometry, which takes into account the liquid metal filled gap between FCI and pipe wall, is shown in Figure 1.

In Figure 2 the electric potential distribution is shown in the lower half of the pipe. The incoming flow is fully developed far upstream with no variations of potential along  $x$  and along magnetic field lines. Here, currents close in cross sectional planes, as shown by current lines displayed in the upper half of the geometry at  $x=x_1, x_2$ . Potential and currents in the other halves

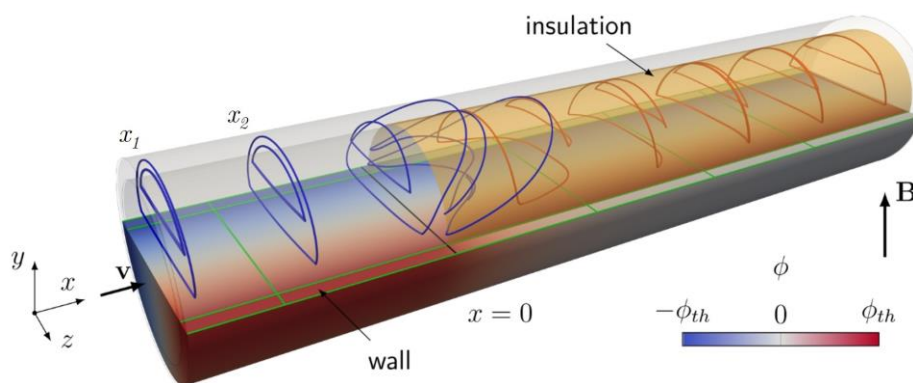


Figure 2 MHD flow entering a FCI for  $Ha=2000, Re=20000$ . Electric potential distribution in the lower half of the pipe and electric current streamlines in the upper half. Current streamlines closing over the wall domain are displayed in blue, while those closing along the FCI are drawn in red. The orange surface represents the insulation layer and the black straight line at  $x=0$  marks its beginning.

of the pipe behave in a  $y$ - symmetric way and they are in agreement with known solutions for fully developed MHD flow under a uniform magnetic field (e.g. [2]).

After entering the FCI for  $x>0$ , the insulation prevents fluid currents from entering the thick-wall domain. They are blocked by the insulation and forced to close along the thin inner sheet of the FCI (red current lines). Far enough downstream, the flow approaches again fully developed conditions.

Three dimensional effects near the FCI entrance at  $x=0$  lead to axial components of current density in the fluid and in the wall. This is caused on one hand by the fact that the potential in the outer wall drops to zero for  $x \gg 1$ , since no currents are supplied to this part of the pipe due to the presence of the insulating layer. The resulting axial potential gradient drives 3D currents in the outer wall, as shown by the strongly bent blue current lines near  $x=0$ . On the other hand, current loops closing along the thin conducting sheet of the FCI experience higher resistance and therefore the potential difference in the cross section is higher than in the well conducting part of the pipe for  $x<0$ . The reason is the significant difference of wall conductivity. 3D effects on currents and potential persist downstream into the FCI over multiple characteristic lengths.

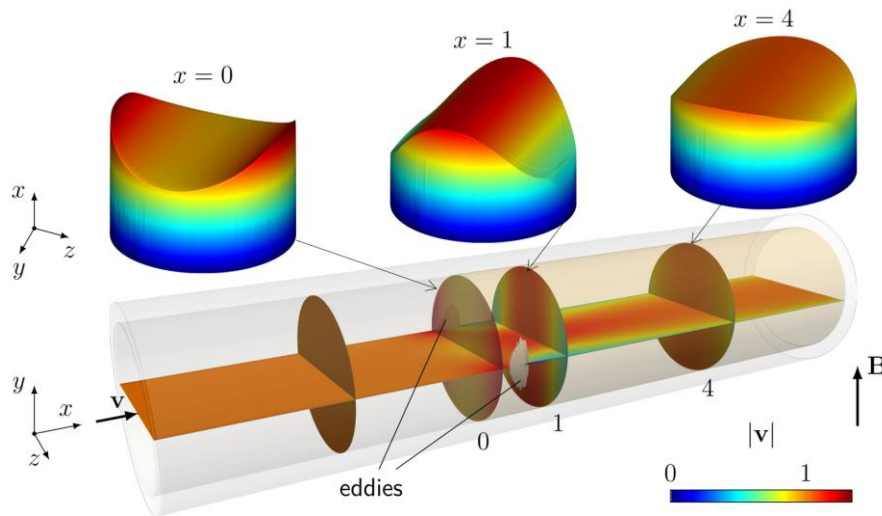


Figure 3 3D profiles of velocity at three axial positions near the entrance of the FCI. The insulation starts at  $x=0$ .

Such complex currents interact with the magnetic field, resulting in Lorentz forces that affect the flow. Figure 3 shows the resulting velocity distribution across the FCI entry region at three axial positions downstream in the FCI. The incoming flow, not shown in the figure, has a uniform core velocity and thin boundary layers along the pipe wall.

As soon as the fluid enters the insulated part ( $x=0$ ), it moves towards the sides forming a concave velocity profile along the transverse  $z$ -direction. This rapidly changes into a convex profile with a center peak ( $x=1$ ). Then, over several characteristic lengths, the velocity slowly converges towards a fully developed flow in the FCI, where the core velocity is almost constant but slightly curved along  $z$ , as displayed at  $x=4$ . Due to the strong velocity gradients in the entrance regions, side layers may become unstable exhibiting locally confined transient eddy regimes between  $0 < x < 1$ .

The pressure distribution in the pipe and FCI is shown in Figure 4 along the axis (blue) and near the sides (red). Pressure gradients in MHD flows in bare pipes and in FCI, as predicted by an asymptotic theory, are marked as straight black lines in the plot. Results from 3D numerical simulations perfectly agree with these theoretical predictions, the vicinity of the FCI entry, center and side pressure separate.

While the transition of the core pressure appears relatively smooth, the pressure near the sides experiences a sharp drop in front of the FCI. Extremely high current densities entering the well conducting wall in front of the FCI result in large Lorentz forces, leading to such high-gradient peaks near the sides. After entering the FCI, the side pressure remains almost constant until leveling off with the core pressure. For ideal fully developed conditions in very long pipes, the relatively low wall conductance of the FCI in comparison to that of the bare pipe wall leads to a significant pressure gradient reduction factor of about 16. 3D MHD phenomena occurring at entrance and exit of FCIs may reduce the efficiency of the insulation due to the additional pressure drop  $\Delta p_{3D}$ , caused by recirculating 3D currents.

While experimental results yield data often extracted from measurements on the outer surface of the pipe [3], the presented numerical investigations provide valuable data and insight into 3D MHD phenomena in the fluid. Computations confirm the FCI's efficiency and show good agreement with asymptotic theory and experimental results.

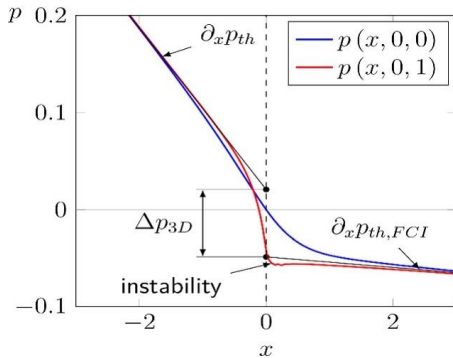


Figure 4 Pressure along the pipe axis (blue) and at the sides (red).

### MHD velocity distribution and pressure drop in manifolds of a WCLL TBM

In the frame of the EUROfusion breeding blanket research activities, the water-cooled lead lithium (WCLL) blanket has been selected as “driver” for a DEMO reactor [4]. Test blanket modules (TBMs) derived from this concept will be tested in the International Thermonuclear Experimental Reactor ITER.

In the present study, liquid metal MHD flows in manifolds of a WCLL TBM have been investigated numerically for different sets of flow parameters.

A view of the WCLL TBM manifold design is shown in Figure 5a. It consists of two long poloidal ducts, electrically connected across a common wall. The liquid metal flows along a series of expansions and contractions due to the presence of horizontal stiffening plates that separate the breeder chambers arranged in a column. This type of MHD flow causes additional pressure drop compared to flow in straight ducts [5]. Liquid metal flows are investigated in the model geometry depicted in Figure 5b, whose dimensions are taken from the most recent WCLL TBM design. A uniform magnetic field is imposed in toroidal direction.

Numerical simulations are performed for periodic fractions of the manifolds by assuming a stepwise decrease/increase of the flow in the

feeding/draining manifolds. Velocity and pressure distributions in the entire manifolds that feed/drain 8 breeder zones are then reconstructed. For all investigated parameters a uniform flow partitioning among BUs (Breeding Unit) has been assumed and flow rates in the manifolds have been derived by taking the same given mean velocity  $u_0$  in all breeding zones. The pressure drop depends linearly on the mean velocity and quadratically on the magnetic field strength. Therefore, results can be extrapolated and scaled, e.g. to other flow rates, depending on design specifications. For the discussion of the results, we consider the manifold as subdivided into eight parts, each corresponding to a specific fed/drained breeding zone (BZ). For that reason the different portions of the manifolds along the poloidal direction are referred to as BZ1,..., BZ8, as indicated in Figure 5a.

Calculations have been carried out by using a finite volume code. Equations describing the MHD flow are implemented in the open source software OpenFoam [6]. Accurate simulations of MHD flows are pretty demanding since they require a proper resolution of thin boundary layers that form along all walls. Their thickness reduces by increasing the intensity of the magnetic field [7]. Moreover, electrically conducting walls provide closing paths for electric currents and their resolution is crucial to determine the total current density in the fluid. About  $4 \cdot 10^6$  nodes are needed in the two fluid domains and  $6 \cdot 7 \cdot 10^6$  in the thick wall to resolve an eighth fraction of the manifold. An example of the computational mesh used for the simulations is depicted in Figure 5c in a toroidal poloidal plane. Simulations have been performed on the HPC MARCONI in Italy by using up to 128 CPUs.

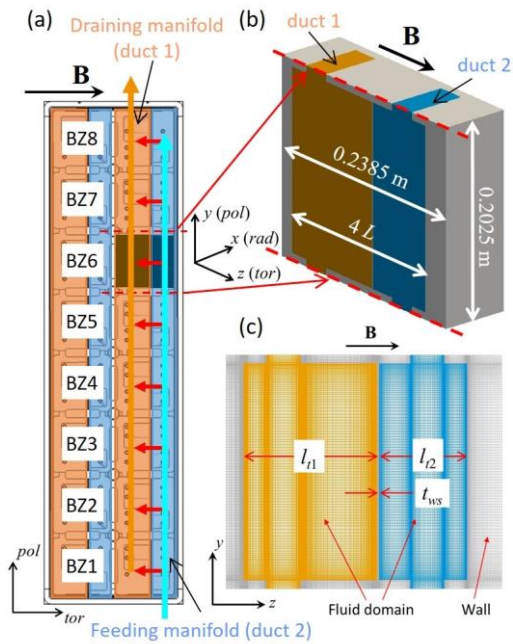


Figure 5 (a) Design of WCLL TBM manifold. Feeding and collecting manifolds are referred to as duct 2 and duct 1, respectively. (b) Periodic fraction of model geometry for numerical analysis. (c) Computational mesh for fluid and wall.

Figure 6 (top) shows, as examples for the flow at  $Ha=4000$  and  $u_0=0.1$  mm/s, 3D views of the velocity distribution at three poloidal locations in the considered geometry at the bottom of the module in BZ1 (a) and in the middle in BZ5 (b). In BZ1 the fluid is supplied to duct 2 (feeding manifold), while the weak flow in duct 1 (collecting manifold) is only driven by electromagnetic coupling caused by leakage currents. In the lower part of Figure 6 the vertical component of the velocity is plotted along the radial white dashed lines in the two channels, as marked in the 3D views. Due to electromagnetic coupling across the common dividing wall the flow in duct 2 pulls that in the core of duct 1 in the same direction. This leads to a buildup of pressure along the flow direction that drives the backward oriented jets in duct 1 (orange curve in Figure 6a at the bottom). In Figure 6b results in the middle portion of the manifolds, BZ5, are displayed. Here the mean velocities in the two coupled ducts are very similar. As a result the velocity distribution is analogous in

both channels. Electric currents induced in the cores of the manifolds enter the corresponding side walls, they flow towards the external and common Hartmann walls through which they pass into the opposite parallel wall. Consequently, no current is exchanged between the two ducts and no significant multichannel effects are observable.

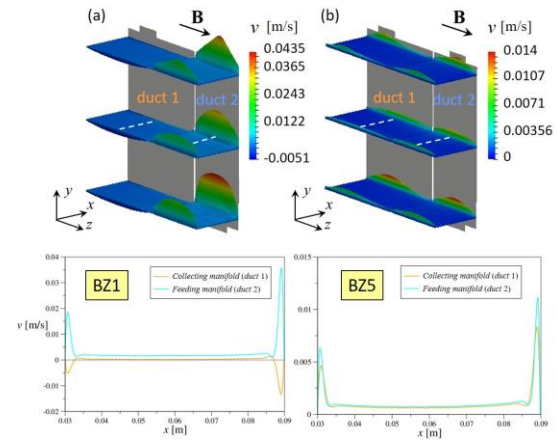


Figure 6 Results for  $Ha=4000$  and  $u_0=0.1$  mm/s, at the bottom of the module in BZ1 (a), in the middle in BZ5 (b). On the upper half of the figure, 3D views of velocity distribution are displayed at three poloidal locations. On the lower half, profiles of vertical velocity are plotted along the radial  $x$  coordinate, as indicated by the white dashed lines.

In Figure 7a the pressure is plotted as a function of the vertical poloidal direction  $y$  along the central line of the ducts forming the manifolds for the flow at  $Ha=4000$  and  $u_0=0.1$  mm/s. The distance between the two curves, marked by red arrows, indicates the pressure difference between feeding and draining manifold, i.e. the available pressure heads between entrance and exit of the corresponding breeder zones. This pressure difference is required to overcome the pressure drop across the windows in the back plate (BP) that connect manifold and BUs, and the one along the breeder zone. Experiments performed to investigate MHD flows in a scaled mock-up of a HCLL blanket showed that the pressure drop in the BUs, is almost negligible compared to the other contributions in the blanket module [8]. The additional pressure drops present at the connections between

two portions of the manifolds, i.e. the steps visible in the pressure distribution in Figure 7a, result from the local 3D MHD effects that occur when the liquid metal expands/contracts along magnetic field lines. For the flow at  $Ha=4000$  and  $u_0=0.1$  mm/s the total pressure drop in the feeding (FM) and collecting (CM) manifolds is given by  $\Delta p_{FM}=0.092$  bar,  $\Delta p_{CM}=0.048$  bar, respectively. The pressure drop in the draining manifold is smaller than the one in the feeding channel because its cross-section is larger.

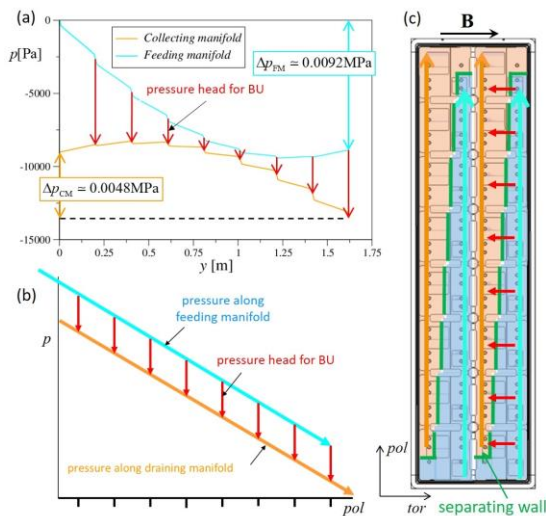


Figure 7 (a) Pressure plotted along the vertical poloidal direction in feeding and draining manifolds for  $Ha=4000$  and  $u_0=0.1$  mm/s. (b) Schematic ideal linear profile of poloidal distribution of pressure in the manifold. (c) Sketch of PbLi path and proposed modification of the manifold design.

In an ideal situation, the pressure heads for each breeding zone should be equal in order to guarantee a uniform flow partitioning among all BUs. However, this would be possible only if the pressure along both manifolds varied linearly and with same slope, as sketched in Figure 7b. In the present manifold design, the cross-sections of the two ducts differ from each other and remain constant along the poloidal length of the module. Consequently, the mean velocity in the feeding manifold becomes smaller along the poloidal direction, when the liquid metal flows from BZ1 to BZ8. Therefore, the pressure gradient decreases. Instead, in

the collecting manifold the flow rate increases along the liquid metal flow path as well as the pressure gradient. The larger pressure head at the external BUs suggests that the flow rate in central BUs is considerably reduced compared to the one at the ends of the module.

Such behavior has been studied in the past by experiments performed in a mock-up of a HCLL TBM [9] and design modifications had been proposed to overcome this undesirable effect. A more uniform partitioning of the liquid metal among the breeding zones could be achieved by adapting the manifold cross-sections to the changing flow rates, so that a constant average velocity is maintained along the liquid metal path, and same pressure head could be reached for each BU. In order to realize these conditions, the vertical wall separating the two manifolds should be moved stepwise in toroidal direction, as proposed in Figure 7c, where the new wall position is drawn in green.

The present numerical study allows for a first estimation of pressure drop in the feeding and in the draining manifolds of a WCLL TBM. Numerical results confirm the typical scaling for the pressure drop in inertialess MHD flows under strong magnetic fields, according to which pressure losses scale linearly with the mean velocity and quadratically with the magnetic field strength,  $\Delta p \sim \sigma L B^2 u_0$ . However, it is still necessary to consider that, even if the pressure drop in the manifolds represents a large part of the total pressure drop in the PbLi system, other contributions should be estimated as well. For instance pressure drops in the long piping system supplying PbLi to the TBM were not part of the present investigation. In these pipes PbLi flows under the action of a spatially varying magnetic field and the velocity is much higher than in the BUs.

The obtained results show that the pressure drop in the manifolds is acceptable for ITER applications. However, a more important aspect is the non-uniform partitioning of the liquid metal flow among different breeding zones due to the geometry of the manifolds in which the

cross-sections do not adjust to the changing flow rates. The proposed modification of the manifold design will be evaluated in future studies.

### Design and fabrication of a WCLL TBM mock-up for MHD experiments

For MHD experiments in the MEKKA laboratory a mock-up of the ITER WCLL TBM has been designed and fabricated (see Figure 8). Objective of these experiments is to achieve knowledge about MHD pressure drop, when the liquid metal flows around obstacles (water pipes) and through contractions and expansions created by stiffening plates in the manifolds and to determine the distribution of PbLi flow among breeder units.

The WCLL mock-up has been 1:2.5 down-scaled to fit into the gap of the magnet at the MEKKA laboratory. Figure 9 shows a transparent CAD view of the mock-up for visualization of the PbLi flow paths.



Figure 8 Manufactured WCLL TBM mock-up.

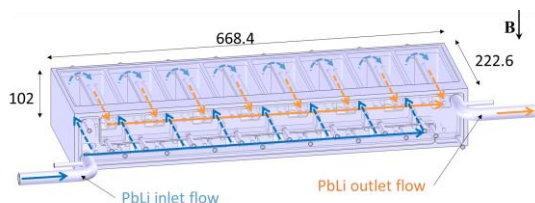


Figure 9 Transparent CAD view with main dimensions (in mm) and PbLi flow paths.

The WCLL mock-up has been simplified to meet manufacturing concerns and to reduce fabrication costs, while keeping the geometry for the liquid metal flow as foreseen in [10]. An exploded CAD view in Figure 10 shows the major parts of the mock-up. The main body consists of a single piece, which forms the walls of all breeder units (BUs), including first wall, stiffening plates, back plate and walls separating the two inlet and outlet manifolds for the PbLi flow. Manifolds are closed by two back plates. Details concerning the water channels inside the blanket walls have been omitted since it should not affect the liquid metal flow. Cooling pipes are all present in the mock-up and simulated by solid dummy elements. All parts are made of 1.4571 austenitic steel that has good compatibility with the used model fluid NaK.

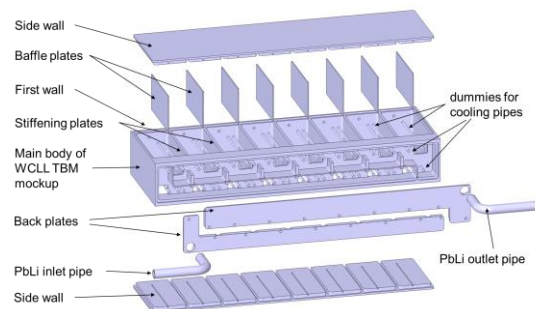


Figure 10 Exploded view of the WCLL MHD mock-up with major components: main body, side walls, back plates as cover for the manifolds, and dummy parts that mimic the water pipes.

The liquid metal is fed into the manifold of the main body and removed from it through circular pipes, which are connected to the existing loop in the laboratory. The PbLi is distributed and collected by two manifolds into and out of the BUs. Each BU is fed through a small window in the back wall of the manifolds. The PbLi flow is redirected at the first wall and guided back into the outlet manifold (see Figure 9).

Pressure differences will be measured between several points of the mock-up using a piping system between pressure taps and the

pressure transducers which are located outside of the magnet. Positions of pressure taps have been chosen to also satisfy the function of feeding, draining and venting (see Figure 12).

Flows in different parts of the module are electrically coupled since currents induced in one part may leak across electrically conducting walls into neighboring channels. Electromagnetic flow coupling and flow partitioning among BUs is investigated by the electric potential distribution on the walls. Experiments using this mock-up in the MEKKA laboratory will start in the second half of 2021.

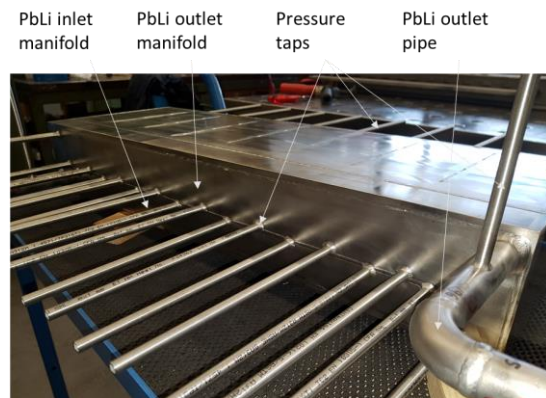


Figure 12 Finalized mock-up.



Figure 11 WCLL TBM mock-up: inlet and outlet manifolds (top), breeder zone with dummies representing cooling pipes, baffle plates and stiffening plates (bottom).

### Reconstruction of 3D velocity profiles from measured surface potential data

Liquid metal pipe flow entering a strong magnetic field had been investigated experimentally and theoretically in a previous campaign [11] [12] using the MEKKA facility [13]. Experimental data for electric potential  $\Phi$  on the external surface of the pipe had been recorded and published in [11]. This data displayed in Figure 13 has been analyzed and potential values  $\phi$  on the fluid-wall interface have been evaluated by solving a sort of inverse problem across the thick-walled pipe. Potential at the fluid-wall interface is of particular interest since it is a result of the interaction of the flow with the magnetic field and from its knowledge it is possible to derive an approximate reconstruction of the velocity distribution in the entire fluid volume.

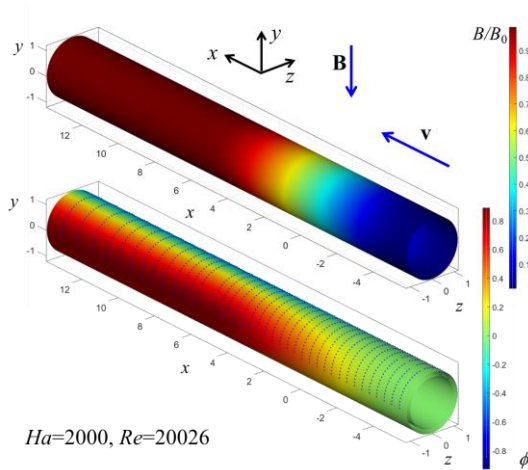


Figure 13 Distribution of magnetic field  $B(x)$  projected to the pipe surface and contours of nondimensional electric potential  $\Phi$  measured on the external surface of the pipe. The positions of the potential sensors are marked by blue dots.

A first step in the analysis is a decomposition of surface data in circumferential Fourier modes

$$\phi(R, \alpha, x) = \Phi(\alpha, x) = \sum F_k(x) \sin(k\alpha),$$

where the nondimensional radius  $R$  denotes the ratio of external to internal radius of the pipe and  $\alpha$  stands for the angle in a polar coordinate system, measured with respect to the magnetic field direction. The  $F_k$  are obtained as best fit of the approach introduced above with the experimental data. Results of  $F_k(x)$  displayed in Figure 14 show that the major physical information is already contained in the first 3 modes while values of mode 5 are already negligibly small.

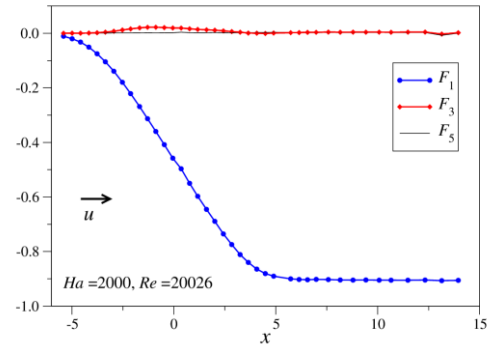


Figure 14 Fourier coefficients  $F_k(x)$  of surface potential  $\Phi(\alpha, x)$  at the external surface of the pipe for  $Ha=2000$ ,  $Re=20000$ .

Assuming a balance between flow-induced electric field  $\mathbf{v} \times \mathbf{B}$  and potential gradient  $\nabla \phi$ , and the fact that the fluid core potential is constant along magnetic field lines [14], we can express the axial component of velocity as

$$u = B^{-1} \frac{\partial \phi}{\partial z} = \frac{1}{B \cos \alpha} \frac{\partial \phi}{\partial \alpha},$$

when  $\phi$  is known in terms of its Fourier expansion. Figure 15 shows velocity contours for the two Hartmann numbers  $Ha=2000$  and  $Ha=5485$ . We observe the formation of increased velocities near the sides  $z \approx \pm 1$  and reduced velocity in the center, in the region where the magnetic field starts rising.

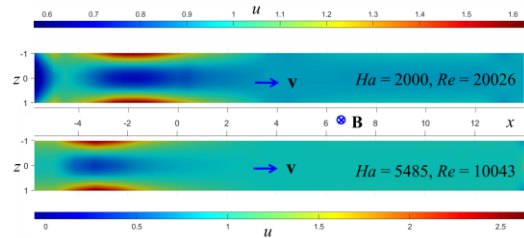


Figure 15 Contours of axial velocity  $u(x, z)$  estimated from measured wall potential for  $Ha=2000$ ,  $Re=20026$  and  $Ha=5485$ ,  $Re=10043$ .

The distributions of axial velocity at the sides  $u(x, z=\pm 1)$  and in the center  $u(x, z=0)$  are plotted in Figure 16. For  $x < -5$ , both the magnetic field and induced potentials are pretty small so that

data evaluation for velocity becomes difficult and the derived data might become unreliable (larger scatter of data for  $x < -5$ ). However, for  $x > -5$  the data shows clear trends. Maximum values reach up to  $u_{\max}=1.62$  and  $2.64$  at  $x \approx -1.68$  and  $x \approx -3.31$  for  $Ha=2000$  and  $Ha=5485$ , respectively.

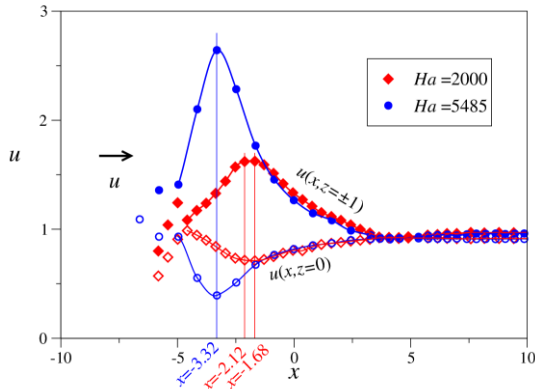


Figure 16 Velocities near the sides (filled symbols)  $u(x, z=\pm 1)$  and in the center (open symbols)  $u(x, z=0)$  for two Hartmann numbers.

It can be observed that the axial position of maximum jet velocity near the sides shifts upstream as the magnetic field  $B_0$  increases. This is most probably caused by the fact that locally the magnetic field increases earlier for higher Hartmann numbers. In order to support this assumption we compare the two experiments in terms of their local Hartmann numbers  $Ha(x)=Ha B(x)/B_0$  as shown in Figure 17, where the two positions of maximum jet velocity have been added to the figure. It can be seen that in both cases the position of maximum jet velocity occurs at almost the same local Hartmann number near  $Ha(x) \approx 560$ . Further downstream, the velocities near the sides decrease slowly and approach that of a uniform core flow with  $u \approx 0.92$ .

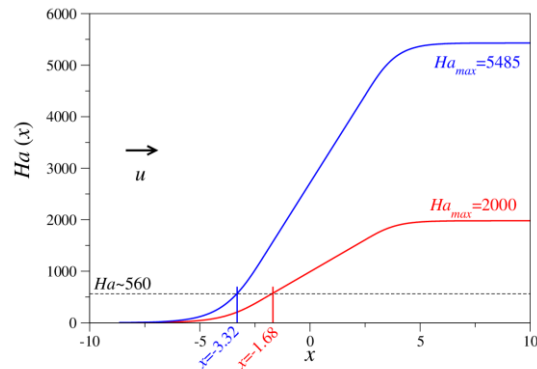


Figure 17 Distribution of local Hartmann number  $Ha(x)$  for the two cases considered. The marked positions  $x=-3.32$  and  $x=-1.68$  denote locations of maximum jet velocity.

The transverse distribution of velocity is shown in Figure 18 for the high Hartmann number  $Ha=5485$  and  $Re=10043$ . We observe high velocity magnitudes near the sides at axial positions where the magnetic field starts rising with a reduced velocity in the center. Further downstream the flow gradually becomes uniform as the magnetic field approached its uniform high magnitude.

The advantage of the presented method for evaluation of velocity from measured potential data is that it yields a global overview of velocity in the entire flow field in contrast to invasive measurements where a probe is traversed along a single line of a cross-section. More details and a discussion about the accuracy of the procedure can be found in [15].

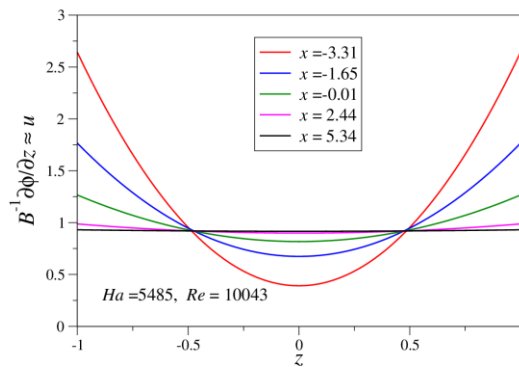


Figure 18 Transverse profiles of axial velocity at different axial positions for  $Ha=5485$  and  $Re=10043$ .

### Experimental study of heat transfer in magneto-convective flows related to WCLL blankets

In WCLL blankets, water-cooled pipes are immersed in the liquid metal to extract the heat from the breeding zone. These pipes generate large thermal gradients within the liquid metal that may lead to quite complex flows governed by the combined effect of buoyancy, electromagnetic force, and pressure gradient. Although some characteristic features associated with such flow have already been identified by numerical studies [16] [17] experimental investigations of magneto-convective flow in prototypical geometries are lacking. Yet, additional studies are required to improve the understanding of this type of flow and support the complex design of a WCLL blanket. To this end, a simplified model geometry was defined with the aim of providing a first experimental database of MHD buoyant flows with heat transfer in WCLL-like geometries.

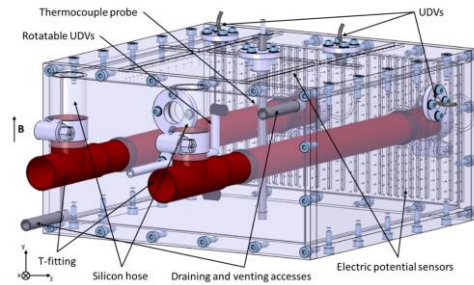


Figure 19 Sketch of the test section.

A sketch of the test section designed to perform magneto-convection experiments in the MEKKA laboratory is shown in Figure 19. It consists of the 200x200x100 mm rectangular cavity made of PEEK plastic through which two parallel horizontal pipes are inserted. Both pipes are connected to their own temperature-controlled water circuits such that they can be kept at constant temperatures  $T_1$  and  $T_2$  to generate the horizontal temperature gradient driving the flow. The pipes are made of copper and they have an inner core to ensure as good isothermal conditions as possible. They are coated with a thin layer (2  $\mu\text{m}$ ) of silicon carbide that provides electrical insulation and prevents corrosion that could occur at higher temperatures in contact with eutectic gallium-indium-tin, which is used as model fluid. The entire test section is instrumented with 71 thermocouples, 416 electrodes and 3 UDV transducers to record simultaneously temperatures, electric potentials at the walls, and velocities. Additionally, flowrates and temperature drop/rise along both pipes are also monitored to evaluate the amount of heat exchanged between the pipes. More details about the test section and the instrumentation can be found in [18].



Figure 20 Photo of the instrumented test section partially thermally insulated before insertion in the magnet gap of the MEKKA laboratory.

Experiments were performed for Hartmann numbers up to 3000 and Grashof numbers ranging from  $2.0 \cdot 10^6$  to  $1.0 \cdot 10^8$ , corresponding to temperature differences  $\Delta T = T_2 - T_1$  imposed between the pipes varying between  $1.4^\circ\text{C}$  and  $69.5^\circ\text{C}$ . Whenever possible, the temperature of the pipes was chosen such that average temperature of the liquid metal  $\bar{T} = (T_2 + T_1)/2$  was close to the temperature inside the magnet gap – set to  $30^\circ\text{C}$  – in an effort to limit as much as possible the external heat exchanges.

The temperature distributions were measured at the center of the box, on the middle of the sidewall (on the heated side,  $z^* = -2.00$ ) and on the back plate ( $x^* = -1.98$ ), as well as on the middle of the top cover ( $y^* = 1.00$ ) and in both pipes. Results obtained are scaled and plot as nondimensional temperature  $T^*$  defined as follow:

$$T^* = \frac{T - \bar{T}}{\Delta T/2}$$

For hydrodynamic experiments, performed in the absence of magnetic field ( $Ha = 0$ ), a convection cell forms in the center of the cavity, between the two pipes. The buoyant flow results in a thermal stratification with the hot fluid staying on the top and the cold fluid on the bottom as seen on the non-dimensional temperature profile measured at the center probe shown in Figure 21.

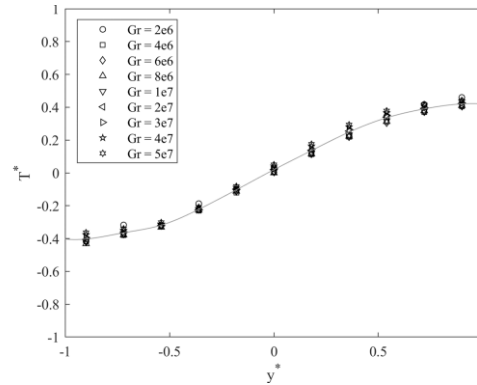


Figure 21 Nondimensional temperature profiles measured at the center of the test section ( $x^* = -0.13$  &  $z^* = 0$ ) for  $Ha = 0$ .

Magnetohydrodynamic experiments exhibit quite different temperature distributions depending on the strength of the applied magnetic field. At the lowest  $Ha$  numbers, the turbulence suppression by the magnetic field first results in larger temperature gradient within the flow (Figure 22), i.e. the thermal stratification becomes stronger. As the magnetic field further increases, the convection motion is damped by the Lorentz forces induced in the liquid metal. Consequently, the vertical thermal gradient at the center of the cavity progressively diminishes until the horizontal thermal stratification has completely disappeared. Eventually, convection motion is so damped that thermal conduction emerges as the dominating heat transfer mechanism and the temperature distribution becomes symmetric with respect to the vertical middle plane of the test section at the highest  $Ha$  numbers.

This result is confirmed by the measurement of the heat transfer coefficient. The intensity of the convective heat transfer has been quantified by deriving the amount of heat released/absorbed at the hot/cold walls, respectively, from the energy balance in both water pipes. The heat fluxes at the pipes can be then evaluated knowing the exchange area and expressed in nondimensional form as Nusselt number

$$Nu = \frac{\dot{m}c_p\Delta T_x L}{\pi d l k (T_{1,2} - \bar{T})}$$

Here,  $\dot{m}$  denotes the mass flow rate of water in the pipe and  $\Delta T_x$  the temperature drop/rise.  $k$  and  $c_p$  are the thermal conductivity of galinstan and the specific heat of water, respectively, and  $d$  and  $l$  are the diameter and length of the pipes (see Figure 23). The characteristic length of the problem  $L$  considered here is half distance between the pipes which is equal to the half size of the box measured along magnetic field lines (Hartmann length).

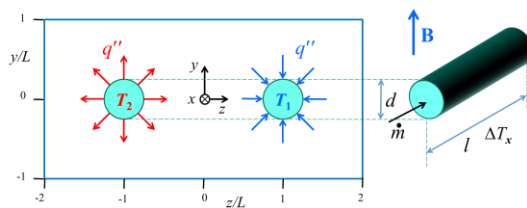


Figure 23 Sketch for the definition of parameters used to derive the Nusselt number.

- For  $50 < Gr/Ha^2 < 4000$ , the intensity of heat transfer increases with  $Gr/Ha^2$ . In this regime, a scaling law has been established such as  $Nu \propto (Gr/Ha^2)^{1/3}$ .

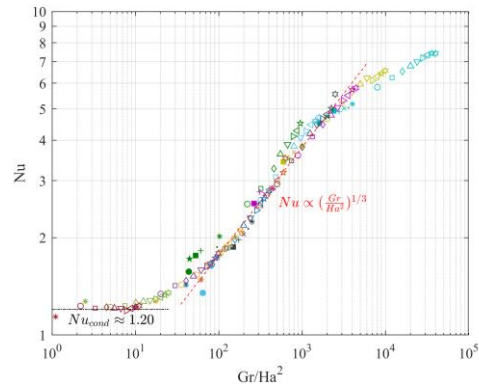


Figure 24 Nusselt numbers measured for several Grashof and Hartmann numbers.

The results are presented in Figure 24 where  $Nu$  is plotted against the quantity  $Gr/Ha^2$  representing the ratio of the buoyancy force over the electromagnetic force. The competition between buoyancy forces, promoting the convection, and the electromagnetic forces, suppressing the flow, lead to 2 distinct heat transfer regimes:

As  $Gr/Ha^2$  grows further, the pace at which  $Nu$  increases slows down and eventually the flow becomes turbulent as proven by current experimental results. While this work already provides valuable data, extended investigation will be carried out focusing on the onset of turbulence in magneto-convective flow.

- For  $Gr/Ha^2 < 10$ ,  $Nu$  is constant and close to unity indicating that heat transfer is purely conductive. Almost all convection motion has been suppressed by the Lorentz force.

### Further work

In addition to the topics described above, the MHD group at ITES KIT contributed in the reporting period 2020 with scientific papers to the

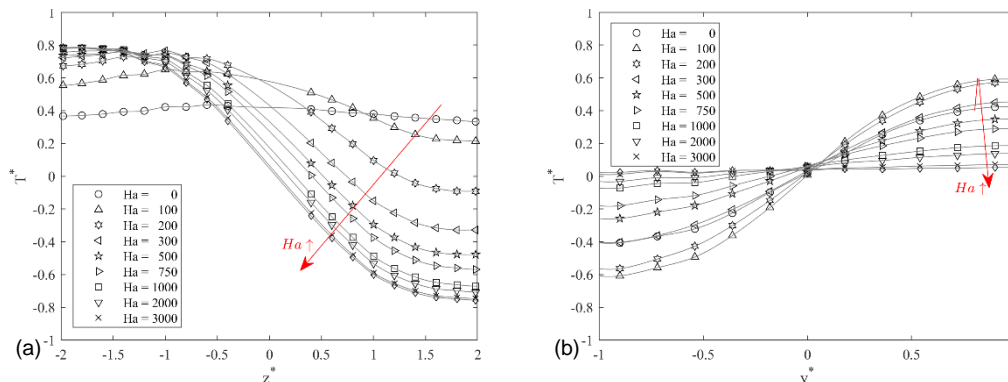


Figure 22 Nondimensional temperature profiles measured for  $Gr=2 \cdot 10^7$  and  $Ha$  ranging from 0 to 3000 (a) on the middle of the top wall ( $x^* = -0.13$  &  $y^* = 1$ ) and (b) at the center of the test section ( $x^* = -0.13$  &  $z^* = 0$ ).

development of fusion technology [19], [20], [21], [22], [23], [24], [25].

**Acknowledgement:** This work has been carried out within the framework of the EUROfusion Consortium and has received funding from the Euratom research and training programme 2014-2018 and 2019-2020 under grant agreement No 633053. The views and opinions expressed herein do not necessarily reflect those of the European Commission.

## References

- [1] Malang, S.; Einrichtung zur Verringerung des MHD-Druckverlustes in dickwandigen Kanälen, Patent DE 36 00 645 C2, 1987.
- [2] Miyazaki, K.; Nakano, M.; Horiba, T.; Inoue S. and Yamaoka, N.; "MHD pressure drop along a NaK flow around a stepwise change of tube diameter under a transverse magnetic field," *Fusion Engineering and Design*, vol. 8, pp. 233-239, 1989.
- [3] Bühler, L.; Mistrangelo C. and Brinkmann, H.-J.; "Experimental investigation of liquid metal MHD flow entering a flow channel insert," *Fusion Engineering and Design*, vol. 154, p. 111484, 2020.
- [4] Federici, G.; Boccaccini, L.; Cismondi, F.; Gasparotto, M.; Poitevin Y. and Ricapito, I.; "An overview of the EU breeding blanket design strategy as an integral part of the DEMO design effort," *Fusion Engineering and Design*, vol. 141, pp. 30-42, 2019.
- [5] Bühler, L.; "A parametric study of 3D MHD flows in expansions of rectangular ducts," *Fusion Science and Technology*, vol. 52, no. 3, pp. 595-602, 2007.
- [6] Mistrangelo, C. and Bühler, L.; "Development of a numerical tool to simulate magnetohydrodynamic interactions of liquid metals with strong applied magnetic fields," *Fusion Science and Technology*, vol. 60, no. 2, pp. 798-803, 2011.
- [7] Smolentsev, S.; Badia, S.; Bhattacharyay, R.; Bühler, L.; Chen, L.; Huang, Q.; Jin, H.-G.; Krasnov, D.; Lee, D.-W.; Mas de les Valls, E.; Mistrangelo, C.; Munipalli, R.; Ni, M.-J.; Pashkevich, D.; Patel, A.; Pulugundla, G.; Satyamurthy, P.; Snegirev, A.; Sviridov, V.; Swain, P.; Zhou T. and Zikanov, O.; "An approach to verification and validation of MHD codes for fusion applications," *Fusion Engineering and Design*, vol. 100, pp. 65-72, 2015.
- [8] Mistrangelo, C. and Bühler, L.; "Magnetohydrodynamic pressure drops in geometric elements forming a HCLL blanket mock-up," *Fusion Engineering and Design*, vol. 86, pp. 2304-2307, 2011.
- [9] Bühler, L.; Mistrangelo, C.; Brinkmann, H.-J. and Koehly, C.; "Pressure distribution in MHD flows in an experimental test-section for a HCLL blanket," *Fusion Engineering and Design*, vol. 127, pp. 168-172, 2018.
- [10] Batal, T.; *Assembly of WCLL TBM: CAD product and parts (by CEA)*., personal communication November 27, 2019.
- [11] Bühler, L.; Brinkmann, H.-J. and Mistrangelo, C.; "Experimental investigation of liquid metal pipe flow in a strong non-uniform magnetic field," *Magnetohydrodynamics*, vol. 56, pp. 81-88, 2020.
- [12] Klüber, V.; Mistrangelo, C. and Bühler, L.; "Numerical simulation of 3D magnetohydrodynamic liquid metal flow in a spatially varying solenoidal magnetic field," *Fusion Engineering and Design*, vol. 156, p. 111659, 2020.
- [13] Barleon, L.; Mack, K.-J. and Stieglitz, R.; "The MEKKA-facility a flexible tool to investigate MHD-flow phenomena," 1996.
- [14] Picologlou, B. F. and Reed, C. B.; "Experimental investigation of 3-D MHD flows

- at high Hartmann number and interaction parameter," in *Liquid Metal Magnetohydrodynamics*, J. Lielpetris and R. Moreau, Eds., Dordrecht, Kluwer, 1989, pp. 71-77.
- [15] Bühler, L. ; Lyu, B.; Brinkmann, H.-J. and Mistrangelo, C.; "Reconstruction of 3D MHD liquid metal velocity from measurements of electric potential on the external surface of a thick-walled pipe," *Fusion Engineering and Design*, vol. 168, p. 112590, 2021.
- [16] Bühler, L. and Mistrangelo, C.; "MHD flow and heat transfer in model geometries for WCLL blankets," *Fusion Engineering and Design*, vol. 122, pp. 919-923, 2017.
- [17] Tassone, A.; Caruso, G.; Giannetti, F. and Nevo, A. D.; "MHD mixed convection flow in the WCLL: heat transfer analysis and cooling system optimization," *Fusion Engineering and Design*, vol. 146, 2019.
- [18] Koehly, C.; Bühler, L. and Mistrangelo, C.; "Design of a test section to analyze magneto-convection effects in WCLL blankets," *Fusion Science and Technology*, vol. 75, pp. 1010-1015, 2019.
- [19] Klüber, V.; Bühler, L. and Mistrangelo, C.; "Numerical investigation of liquid metal flow in square channels under inclined magnetic fields for fusion relevant parameters," *Magnetohydrodynamics*, vol. 56, pp. 149-156, 2020.
- [20] Mistrangelo, C.; Bühler, L.; Smolentsev, S.; Klüber, V.; Maione, I. and Aubert, J.; "MHD flow in liquid metal blankets: major design issues, numerical analysis and code validation," in *Invited talk at the 31st Symposium on Fusion Technology (SOFT2020)*, Virtual edition, 2020.
- [21] Mistrangelo, C.; Bühler, L. and Klüber, V.; "Three-dimensional magneto convective flows in geometries relevant for DCLL blankets," *Fusion Engineering and Design*, vol. 159, p. 111686, 2020.
- [22] Mistrangelo, C.; Bühler, L.; Smolentsev, S.; Klüber, V.; Maione, I. and Aubert, J.; "MHD flow in liquid metal blankets: major design issues, MHD guidelines and numerical analysis," *Fusion Engineering and Design*, p. accepted, 2021.
- [23] Mistrangelo, C.; Bühler, L.; Koehly, C. and Ricipito, I.; "Magnetohydrodynamic velocity and pressure drop in WCLL TBM," in *Proceedings of the 28th IAEA Fusion Energy Conference, May 10-15, Virtual*, 2021.
- [24] Mistrangelo, C.; Bühler, L.; Koehly, C. and Ricipito, I.; "Magnetohydrodynamic velocity and pressure drop in WCLL TBM," *Nuclear Fusion*, p. in print, 2021.
- [25] Smolentsev, S.; Rhodes, T.; Yan, Y.; Tassone, A.; Mistrangelo, C.; Bühler, L. and Ugorri, F. R.; "Code-to-code comparison for a PbLi mixed-convection MHD flow," *Fusion Science and Technology*, vol. 76, pp. 653-669, 2020.